

Response to reviewers

Reviewer 1

A point that remains unclear is the dependence of the modelling results on the choice of finite elements. The authors discuss it in their revisions, but they do not address that the difference they observe appears to be larger than the 10% found in the study they cite. Why is that? I don't think that the issue of "how is it possible to compare the results of one geometry to another?" raised by the other reviewer has been fully addressed.

The 10% difference in stress values cited in Dumont et al (2005) compared two types of element that were the same shape but possessed different numbers of nodes – 4-noded lower-order elements with a node on each apex of the tetrahedral, and higher order 10 node elements, with a node on each apex and along each edge. Here we refer to the difference between two types of element of different shape – tetrahedral versus hexagonal. We have made the nature of our comparison clearer in the text, and that a difference greater than 10% may be due to different element shapes. Why this should be the case is beyond the scope of this study, but we account for this issue by meshing all our models with 4-noded linear elements to ensure comparable results.

Please find our addition to the text below

Page 10 Line 194

Whereas [Dumont et al. \(2005\)](#) found that comparing a converged 4-node linear and a stiffer 10-node quadrilateral tetrahedral mesh of the same model gave different mean stress values, but within 10%. This shows that even when comparing different forms of the same tetrahedral element, variation in stress is still apparent. Hence when comparing different element types (hexagonal and tetrahedral), we find an even greater difference in variation. Therefore in order to compare the 2D to 3D geometric models, the corridor model was meshed with 4- node linear hexagonal elements. As tetrahedral elements were better at capturing the complex geometry of the biological model and to account for variation in results depending on element type, all models were then meshed with 4-node linear tetrahedral elements in order to be compared to the biologically realistic model and to each other.

minor edits:

- *is affiliation 3 used?*

We have added affiliation 3.

- *abstract: consider rewording "models that represent ... growth" to models that represent different structures*

Page 2 line 22

We have changed the text to "*different aspects of coralline algal growth*" as we felt this was a more accurate representation than *structures*.

- *specify values and sources of Cd and A used to arrive at a drag force of 0.9N (line 259)*

We have added the Algal planform area and the source of the drag force, however as the drag force was measured and not calculated the drag coefficient wasn't needed to derive the drag force. We have reworded the line in the text to reflect this.

Page 12 Line 259

Hence, we used a drag force (0.9N) measured for a heavily branched macroalgae (similar in branching to our rhodoliths) with an algal planform area of 48.20 cm² that experienced a wave velocity of 3.5 m s⁻¹ to carry out our load type comparison tests ([Starko et al., 2015](#)).

- consider adding an explanation why 'the compartment model was not able to run', or what issues were encountered (line 318)

We have added an explanation

Page 16 Line 325.

The compartment model did not run under the sole shear load as it experienced extremely high stresses at the interface between the bottom constraint and the adjacent unconstrained surface.

Reviewer 2

*There's a typo in figure 4. The full thickness of the cell wall in the x axis should be 2.68 in order that the x distances sum correctly - $10*5.15 + 9*2.68 + 2*1.34 = 78.30$*

This has been amended.

1 Potential and Limitations of Finite Element Modelling in Assessing Structural Integrity of
2 Coralline Algae under Future Global Change

3 Running head: Modelling the coralline algal skeleton

4 L.A. Melbourne^{1,2,3}, J. Griffin¹, D.N. Schmidt¹ and E.J. Rayfield²

5 1) School of Earth Sciences, University of Bristol, Wills Memorial Building, Queen's
6 Road, BS8 1RJ, Bristol, UK

7 2) School of Earth Sciences, University of Bristol, Life Sciences Building, 24 Tyndall
8 Avenue, BS8 1TQ, Bristol, UK

9 3) Department of Life Sciences, Natural History Museum, Cromwell Road, SW7 5BD,
10 London, UK

11

12 Corresponding Author: Leanne Melbourne, tel +44 (0) 117 954 5243, fax +44 (0)117 954
13 5420, email: l.melbourne@bristol.ac.uk

14 ABSTRACT

15 Coralline algae are important habitat formers found on all rocky shores. While the impact of
16 future ocean acidification on the physiological performance of the species has been well
17 studied, little research has focussed on potential changes in structural integrity in response to
18 climate change. A previous study using 2D Finite Element Analysis (FEA), suggested
19 increased vulnerability to fracture (by wave action or boring) in algae grown under high CO₂
20 conditions. To assess how realistically 2D simplified models represent structural
21 performance, a series of increasingly biologically accurate 3D FE-models that represent
22 different aspects of coralline algal growth were developed. Simplified geometric 3D models
23 of the genus *Lithothamnion* were compared to models created from computed tomography
24 (CT) scan data of the same genus. The biologically accurate model and the simplified
25 geometric model representing individual cells had similar average stresses and stress
26 distributions, emphasizing the importance of the cell walls in dissipating the stress throughout
27 the structure. In contrast models without the accurate representation of the cell geometry
28 resulted in larger stress and strain results. Our more complex 3D model reiterated the
29 potential of climate change to diminish the structural integrity of the organism. This suggests
30 that under future environmental conditions the weakening of the coralline algal skeleton
31 along with increased external pressures (wave and bioerosion) may negatively influence the
32 ability for coralline algae to maintain a habitat able to sustain high levels of biodiversity.

33 **1 INTRODUCTION**

34 Since the pre-industrial era CO₂ concentrations have risen by more than 100ppm (Ciais et al.,
35 2013). The ocean has absorbed approximately 30% of the total anthropogenic CO₂ emissions
36 (Rhein et al., 2013). This has led to a change in the carbonate chemistry of the ocean,
37 resulting in a lowering of the carbonate saturation state and a decrease in ocean pH, a process
38 termed ‘ocean acidification’ (Caldeira and Wickett, 2003). Future projections suggest an
39 additional average decrease in pH of between 0.13 (RCP 2.6) and 0.42 units (RCP 8.5) by the
40 year 2100 (Pörtner et al., 2014). Calcifying organisms are at risk as the lower carbonate
41 saturation state may affect the ability to calcify shells and skeletons (Diaz-Pulido et al., 2011;
42 Fabricius et al., 2011; Kroeker et al., 2010). In response, ecosystem shifts are predicted to
43 occur; for example sea-grasses and kelps may outcompete calcifying algae as the major
44 habitat formers in shallow water habitats (Fabricius et al., 2011).

45 Rhodoliths (Fig. 1), non-geniculate free living (live and dead) coralline red algae (Foster,
46 2001), are an extremely diverse group of benthic calcifying organisms found from the polar
47 to the tropical regions and low intertidal zones to 150m deep (Foster, 2001). They are major
48 contributors to the global inorganic carbon budget in shallow water ecosystems (Mackenzie
49 et al., 2004). The largest rhodolith bed found on the Abrolhos shelf contributes roughly 5% to
50 the global calcium carbonate budget (Amado-Filho et al., 2012). Additionally these benthic
51 ecosystems support a high level of biodiversity by forming structurally and functionally
52 complex habitats (Nelson, 2009) for many organisms including polychaetes, crustaceans and
53 molluscs (Foster, 2001), as well as being important nursery grounds to commercial species
54 including scallops (Grall and Hall-Spencer, 2003). Coralline algae biodiversity and habitat
55 complexity are directly correlated; species richness and abundance of, in particular,
56 arthropods, annelids and cnidarians, are known to increase as rhodolith size and branching
57 increases (Foster et al., 2013). However coralline algae are ecologically fragile due to their

58 slow growth rate of $\sim 1\text{mm yr}^{-1}$ (Freiwald and Henrich, 1994) and sensitivity to physical
59 disturbances such as extraction and dredging.

60 Furthermore, as they form high Mg- calcite skeletons, the most soluble polymorph of calcium
61 carbonate (CaCO_3) (Andersson et al., 2008), coralline algae are more susceptible to ocean
62 acidification than other organisms that utilise different polymorphs of calcium carbonate.
63 Consequently, a significant loss of rhodoliths from the North Atlantic by the year 2100 has
64 been predicted (Brodie et al., 2014). However, laboratory experiments have shown highly
65 varied responses to elevated levels of CO_2 . Coralline algae (*Neogoniolithon* sp.) and
66 calcareous green algae (*Halimeda incrassata*) exposed to increased CO_2 concentrations (606
67 and 903 ppm for 60 days) showed an increase in calcification (Ries et al., 2009); whereas
68 another study on *Lithothamnion glaciale*, a cold temperate coralline algae, displayed a
69 decrease in growth rate at elevated CO_2 conditions (589 and 755 μatm for three months)
70 (Ragazzola et al., 2012), while also showing evidence for potential acclimation after ten
71 months (Ragazzola et al., 2013).

72 Coralline algae have many pressures to withstand in their natural environments, including
73 wave action and bioerosion, while maintaining a structurally and functionally complex
74 habitat. Under elevated CO_2 conditions the algal skeleton appeared to be weakened
75 (Ragazzola et al., 2012), thereby favouring erosion and breakage (Kamenos et al., 2013;
76 Ragazzola et al., 2012).

77 Finite Element Analysis (FEA) is a technique that reconstructs the stress, strain and
78 deformation in structures (Zienkiewicz et al., 2005). Originally developed for mathematical
79 and engineering applications, it has recently become an established technique in zoology and
80 palaeontology to understand morphology, function and evolution of hard tissue structures
81 (Rayfield, 2007).

82 FEA works by transforming a continuous structure into a discrete number of elements which
83 are connected to each other via nodes. The combination of elements and the interconnecting
84 nodes form the mesh. Appropriate material properties (Young's modulus and Poisson's ratio)
85 are assigned to the elements to mimic the elasticity of the structure. Adequate boundary
86 conditions (magnitude and direction of loading and constraints) are applied and then nodal
87 displacements are calculated in response to the applied boundary conditions and material
88 properties of the model. The nodal displacement is used to calculate the strain and
89 subsequently stress (using the Young's modulus, see equation 1) and hence mechanical
90 performance of complex structures can be inferred. (For mathematical equations see
91 Mathematics of FEA, (Rayfield, 2007) supplementary material)

$$92 \quad E \text{ (Young's modulus)} = \sigma \text{ (stress)} / \varepsilon \text{ (Strain)} \quad (1)$$

93 Ragazzola et al. (2012) were the first to use FEA in ocean acidification studies by creating
94 simple 2D FE-models of coralline algae to quantify the effect of elevated CO₂ on the skeleton
95 of *Lithothamnion glaciale*. Although the changes in growth rate were not significant,
96 specimens grown under CO₂ conditions predicted for the year 2050 were found to have
97 significantly larger cells and thinner cell walls. These ultrastructure changes resulted in
98 predicted increased vulnerability to fracture compared to present day structures (Fig. 2a-b) as
99 observed in the 2D FE-model.

100 These simple 2D models represented the mechanical performance of a cross-section of
101 uniform thickness (1µm) (Ragazzola et al., 2012) through the algal structure. However, these
102 highly innovative models were simplistic in nature. Importantly, they had not been tested to
103 assess if they were a fair representation of skeletal mechanical performance. Consequently,
104 the simple 2D model may have overestimated the distribution and magnitude of stress and
105 hence future vulnerability of algal communities. Here we have developed a set of 3D FE

106 geometric models to represent different aspects of coralline algae morphology and compared
107 these models with a more biologically accurate 3D FE-model generated from computed
108 tomography (CT) data, allowing us to assess the trade-off between computing time (Andersen
109 and Jones, 2006; Romeed et al., 2006) and the need for an appropriate representation of the
110 structure.

111 We then used our improved understanding of the performance of the 3D models to re-assess
112 the impact of current and future ppm CO₂ induced changes to morphology on the ability of
113 algal communities in maintaining a high level of biodiversity. Finally, the loading and
114 constraint taken from Ragazzola et al. (2012) were a mixture of shear and compressive
115 forces, which simulated boring forces by an organism exerted on the exposed corner of an
116 attached thallus. As it was assumed that these organisms were more prone to shear forces
117 than compressive ones, we also assessed the effect of sole compressive or sole shear forces
118 on the compartmentalised and the biologically realistic model.

119 **2 MATERIALS AND METHODS**

120 **2.1 Model Geometry**

121 Four 3D FE-models with different coralline algal features were created based on the
122 measurements and properties of Ragazzola et al. (2012) models. All 3D geometric models
123 were created and analysed in the Finite Element software package, Abaqus/CAE, v.6.10,
124 (Simula, USA, Dassault Systèmes, //Simula, Providence, RI, USA), following the protocol
125 established by Ragazzola et al (2012).

126 Firstly, the 2D models from Ragazzola et al. (2012) were expanded, using the extrude
127 command in Abaqus, to create a 3D model with the same area, all length and width
128 dimensions (78.92 x 72.46 μm) were unchanged, but a depth of 80 μm was used instead of 1
129 μm . Size of the individual cells mirrored that of the 422 μatm model of Ragazzola et al.
130 (2012), with an individual cell height of 6.3 μm and width of 5.15 μm and an inter- and intra-
131 wall thicknesses of 2.68 μm and 0.86 μm respectively. This structure is assigned the label
132 ‘Corridor model’ (Fig. 3a). The inter-wall thickness was the thickness of a single cell wall in
133 the x direction (between filaments). Therefore the internal walls of the model had two inter
134 cell walls, whereas the external walls (the left outermost and right outermost) only had one
135 inter cell wall each. The intra-cell thickness was the cell wall thickness between cells in the
136 y-direction. As the rhodolith grows as a set of filaments, there was only one cell wall between
137 two cells in the y-direction (Fig.4).

138 **2.1.1 Compartmentalised (Individual Cell) model with current/ 422 μatm CO₂ cell size**

139 Although the cellular width and height in the Corridor model represented the dimensions
140 recorded by Ragazzola et al. (2012) from SEM images, the cells are not represented as
141 discrete entities and instead are represented as hollow calcite ‘tubes’. As algal cells grow
142 apically, they form a lattice of individual cells, hence a second model, ‘Compartment model’
143 (Fig. 3b) was created in which cell walls were added in the Z direction to create discrete

144 cellular spaces. All dimensions apart from the depth of the individual cells and divisions
145 between cells in the z direction were the same as the corridor model. It was assumed the
146 depth of the cell was the same as the width (5.15 μm) and the divisions between the cells in
147 the z direction were the same as the inter cell wall divisions (2.68 μm).

148 **2.1.2 Biologically realistic model**

149 Computed tomography (CT) scans of *L. glaciale* derived from the TOMCAT beamline at the
150 Swiss Light source, Switzerland (see Ragazzola et al, 2012) were imported into *Avizo* V8.0
151 (VSG) software package. Each scan was 150 projections over 180° using a 15 keV energy
152 beam with UPLAPO 10x objective. The field of view was 1.5 x 1.5mm² and the pixel size
153 was 0.74 x 0.74 mm². A 3D cube of similar dimensions (80 x 80 x 80 μm) as the geometric
154 models was created but instead capturing the actual morphology of the rhodolith (known as
155 the ‘Biological model’) (Fig. 3c). The cube was selected at random within the scan of the
156 rhodolith (Fig. 5 a-d), as the summer winter layers could not be distinguished in the CT scan.
157 The scans were thresholded in *Avizo* and then exported to *Hypermesh* (v.11; part of the
158 *Hyperworks* package from Altair, MI, USA) to create FE-models, which were analysed in
159 *Abaqus* v6.10.

160 **2.1.3 Compartmentalised (Individual Cell) model with 2050 / 589 μatm CO₂ cellular** 161 **size**

162 A final model, ‘the OA model’ (Fig. 3d), was created by adjusting the cell size and spacing to
163 represent the dimensions of the future 589 μatm CO₂ model as a 3D and compartmentalised
164 structure with overall dimensions (74.99 x 77.2 x 80 μm), individual cell dimensions (11.7 x
165 7.99 x 7.99 μm) and intra and inter-cell wall dimensions (0.685 μm and 0.829 μm
166 respectively). This future predicted CO₂ model was compared to the performance of the 3D
167 compartment model with current CO₂ ppm cell size.

168 **2.2 Finite element analysis (FEA)**

169 **2.2.1 Boundary conditions**

170 In keeping with Ragazzola et al. (2012), a load pressure of 20,000 Pa was applied to the top
171 left corner, 40 μm along the external top surface and 40 μm down the left surface of the
172 models. Constraints were applied to the whole bottom surface and on the right hand surface,
173 opposite the loads, 40 μm up from the constrained bottom (Fig. 6). This simulated the
174 attachment of the structure to the rest of the thallus. Even though the same loads as Ragazzola
175 et al. (2012) were used, it is known that the primary hydrodynamic force exerted on marine
176 macroalgae is drag force (Carrington, 1990). Drag (F_{drag}) force can be calculated using
177 equation 2.

$$178 \quad F_{\text{drag}} = \frac{1}{2}(\rho U^2 A C_d) \quad (2)$$

179 Where ρ is the seawater density (approximately 1025 kg m^{-3}); and U is water velocity.
180 Subtidal marine macroalgae experience a water velocity on the order of magnitude of 1 m s^{-1}
181 (Carrington, 1990), while intertidal species can experience breaking waves of up to 25 m s^{-1}
182 (Denny et al., 2003). A is the algal planform area; and C_d the drag coefficient (dimensionless
183 index of shape change and reconfiguration of flexible fronds (Carrington, 1990; Dudgeon and
184 Johnson, 1992; Gaylord et al., 1994)). However, there are no data published for resulting in
185 breakage of rhodoliths, instead the existing literature focused on flexible macroalgae, making
186 it difficult to find loads that are environmentally significant whilst also being species related.

187 **2.2.2 Element type and size**

188 Convergence tests were performed for each mesh type in order to determine the minimum
189 mesh size required. The mesh size was decreased until the average von Mises value no longer
190 changed relative to mesh size. Hypothetically, all refined meshes should converge to similar
191 results yet our converged von Mises stress value was an order of magnitude different between
192 the hexagonal and tetrahedral mesh. This was due to the shape of the tetrahedral elements and

193 the way tetrahedral elements interlock together, making a tetrahedral model stiffer than a
194 hexagonal model. Whereas Dumont et al. (2005) found that comparing a converged 4-node
195 linear and a stiffer 10-node quadrilateral tetrahedral mesh of the same model gave different
196 mean stress values, but within 10%. This shows that even when comparing different forms of
197 the same tetrahedral element, variation in stress is still apparent. Hence when comparing
198 different element types (hexagonal and tetrahedral), we find an even greater difference in
199 variation. Therefore in order to compare the 2D to 3D geometric models, the corridor model
200 was meshed with 4- node linear hexagonal elements. As tetrahedral elements were better at
201 capturing the complex geometry of the biological model and to account for variation in
202 results depending on element type, all models were then meshed with 4-node linear
203 tetrahedral elements in order to be compared to the biologically realistic model and to each
204 other.

205 **2.2.3 Material Properties**

206 In keeping with Ragazzola et al. (2012), all models were assumed to be composed of a
207 linearly elastic, isotropic, homogeneous material with a Young's Modulus of 36 GPa and a
208 Poisson ratio of 0.31 (properties of calcite) (Tanur et al., 2010). Even though these material
209 properties do not accurately represent the heterogeneities in the specimen and their material
210 properties this approach gives a comparative insight into how different geometries affect the
211 overall strength of a structure.

212 Initially, to analyse how sensitive the models were to changing material properties, a set of
213 2D and 3D corridor models with different Young's modulus (maximum and minimum
214 Young's modulus values of two different bivalves – *Mytilus edulis* and *M. californianus*)
215 were analysed.

216 **2.2.4 Displaying and recording results**

217 In order to compare the impact of predators on the different 3D geometric models, stress and
218 strain results were calculated. Stress, generated by the applied load (force) on a given area, is
219 represented by the von Mises stress, a function of each of the principle stresses that represents
220 tensile or compressive stress (Rayfield, 2007). Average stresses were calculated by dividing
221 the von Mises stress by the element size to account for differing number of elements between
222 models. Total strain energy refers to the energy stored in a system as a load is applied, which
223 is a useful variable to record in mineralized structures as the more strain in a system leads to a
224 larger amount of potential energy available for fracture (Gordon, 1978). The 95th percentile of
225 (Mises) stress was additionally used as a comparison between the corridor, compartment and
226 biological models as this metric highlighted the extremes of the von Mises Stress distribution
227 – an important parameter to highlight fracture potential.

228 Stress and strain energy are linearly dependent on surface area and volume respectively
229 (Dumont et al., 2009), hence the applied pressure was rescaled for the biological model to
230 rule out the effect of increased Mg-calcite volume on modelling stress and strain. To account
231 for the increase in volume of calcite between the 2D and the 3D model, as strain energy is
232 dependent on volume, the strain energy was calculated for the 3D model using equation 3,
233 outlined by Dumont et al. (2009);

$$234 \quad U_{B^*} = (V_B/V_A)^{1/3} (F_A/F_B)^2 U_B \quad (3)$$

235 where U_{B^*} is the total strain energy for model B corrected for calcite volume, V_A and V_B are
236 the volumes for the models A and B respectively, F_A and F_B are the loads applied to the two
237 models and U_B is the total strain energy for model B.

238 The von Mises stress was displayed graphically on the model, with warm colours
239 (red/orange) indicating areas of high stress and cool colours (blue) indicating areas of low

240 stress. Stress distribution throughout the model was very similar to surface stress distribution.
241 The surfaces of the model were more sensitive to the loads and constraints, due to immediate
242 contact with the boundary conditions. The minimum and maximum von Mises stress values
243 were found on the surfaces of the models, being more influenced by the position of the
244 boundary conditions and complexities in the geometry. Hence, the minimum and maximum
245 values did not provide any additional information on the overall structural integrity of the
246 model than that provided by the surface contour plots. Average stress values, total strain
247 energies and 95th percentile of (Mises) stress can be found in Table 1.

248 **2.3 Comparison between shear and compressive loading**

249 The biological and the compartment model were exposed to different loading scenarios in
250 Abaqus. This included the original load setup explained earlier in section 2.1.4 (Fig. 7a); the
251 compressive loads, where the load was applied to the top of the cube opposite the constraint
252 (Fig. 7b); and shear loads, where the load was applied on the face adjacent to the bottom
253 constraint (Fig. 7c).

254 As this part of the study moved on from the initial research of Ragazzola et al. (2012), it was
255 decided to use loads defined experimentally based on real wave velocities. Starko et al.
256 (2015) used wave velocities of up to 3.5 m s^{-1} to assess the effect of branching in flexible
257 wave swept macroalgae, in which they also measured the drag force. Water velocity
258 experienced by subtidal marine macroalgae is on the order of magnitude of 1 m s^{-1}
259 (Carrington, 1990). Hence, we used a drag force (0.9N) measured for a heavily branched
260 macroalgae (similar in branching to our rhodoliths) with an algal planform area of 48.20 cm^2
261 that experienced a wave velocity of 3.5 m s^{-1} to carry out our load type comparison tests
262 (Starko et al., 2015). Here we have kept the force per unit area constant in order to compare
263 the compartment model to the biological model. Strain energy is dependent on volume,
264 therefore in order to compare the total strain energy between the models we had to take into

265 account the difference in calcite volume between the biological model and the compartment
266 model (using equation 3) (Dumont et al., 2009).

267 **3 RESULTS**

268 A similar stress distribution was observed in the 2D and 3D geometric model (Corridor
269 model) (Fig. 8a-b), with areas of high stress occurring along the intra-cell walls and adjacent
270 to the constrained surface. The average von Mises stress of the two models was very similar
271 (Table 1), indicating that the simple 2D model (Fig. 8a) was an accurate representation of the
272 stress in a simple 3D geometric model (Fig. 8b). As expected, the total strain energy in the
273 3D model was over 500x higher than the 2D model, showing that the 3D model with a larger
274 volume was able to store more than the relative amount of strain energy compared to the 2D
275 model.

276 Once the complexity of the 3D model was increased to better represent the natural structural
277 complexity, differences between the simple 3D model (Corridor model) and the more
278 complex models became evident (Fig. 9a-c). In the compartment model of current CO₂
279 conditions (Fig. 9b), both, the average stress and total strain energies were lower than the
280 Corridor model (63% and 76% respectively) (Table 1). The addition of cellular walls in the Z
281 direction removed regions of peak stress near the constraints as stresses now dissipated
282 throughout the structure, stabilising the model.

283 The results of the comparison between the 3D geometric models (the Corridor and
284 Compartment model) and the realistic model of similar dimensions generated from CT scans
285 (the Biological model) showed that a similar average stress, strain energy (Table 1) and stress
286 distribution (Fig. 9b-c) was observed between the compartment model and the biological
287 model. Comparison of the internal morphology between the compartment model and the
288 biological model also showed similarities. Both models had regularly distributed cavities.
289 However unlike the compartment model the biological model cavities were spheroidal and,
290 due to the natural variation within these specimens, the arrangement of cavities was not as
291 regimented as in the compartment model (Fig. 10). Both the biological model and the

292 compartment model had the same percentage volumes of calcite and cavities whereas the
293 corridor model had a lower percentage volume of calcite (Table 2).

294 As the compartment model was similar in performance to the biological model, we used this
295 model to assess the impact of ocean acidification (Fig. 2c-d). The change in wall thickness
296 and cell size in the 589 μatm / 2050 model led to a near doubling of average stress and a
297 doubling of the total strain energy (Table 1). This increase in strain energy was less than
298 suggested using the simple 2D models, which predicted an increase in average stress of 309%
299 and strain energy of 1421%.

300 However, using more environmentally significant forces in the shear and compressive
301 comparison tests, we can see that the stresses and strains exerted by these organisms were not
302 as large as those taken from Ragazzola et al. (2012). Accounting for the change in units, the
303 differences between the von Mises stress results (Pa) are on the order of magnitude of 10^9
304 instead of 10^{11} .

305 In the biological model, under the original load setup, stress dissipated throughout the model
306 from the corner where the load was applied to the constrained corner (Fig. 7a). While under
307 the compressive load setup, the stress had a top to bottom distribution (from the loaded
308 surface to the constrained surface) with a slight increase in stress surrounding the cavities in
309 the model (Fig. 7b) and under the shear load setup, two thin bands of higher stress
310 perpendicular to each other were observed (Fig. 7c). The average von Mises Stress, 95th
311 percentile of (Mises) stress and total strain energy were slightly larger under the shear load
312 setup compared to the compressive load setup (Table 3). All three values were larger than the
313 compressive or shear model in the original load set up (Table 3).

314 In the compartment model, under the original load setup the stress dissipated throughout the
315 model from the corner where the load was applied to the constrained corner (Fig. 7d). While

316 under the compressive load setup, the area of higher stress was restricted to the top of the
317 model where the load was applied (Fig. 7e) and under the shear load setup, the area of high
318 stress spread from the right hand side near the constrained corner (Fig. 7f). The average von
319 Mises stress, 95th percentile of (Mises) stress and the total strain energy were largest under
320 sole shear loads and smallest in the compressive load model, with values for the original set
321 up falling in between (Table 3).

322 Note the shear load in the compartment model was applied differently to the arrangement for
323 the biological model. As the compartment model was not able to run under a sole shear load,
324 like the biological model, a small constraint on the opposite face (1 μ m) was added to help
325 stabilise the model (Fig. 7f). The compartment model did not run under the sole shear load as
326 it experienced extremely high stresses at the interface between the bottom constraint and the
327 adjacent unconstrained surface.

328 The sensitivity test of the 2D model and the 3D corridor model highlighted that increasing the
329 Young's modulus by 120% did not result in any change in stress, whereas the total strain
330 energy decreased with increasing Young's modulus (Table 4).

331 **4 DISCUSSION**

332 Ragazzola et al. (2012) used 2D FE-models to predict if changes to coralline algae cellular
333 morphology induced by higher CO₂ concentrations generate a structure that might less able
334 withstand stresses compared to current specimens. They predicted that increased CO₂ and
335 resulting ocean acidification will create a structure more susceptible to fracture in response to
336 environmental stressors such as wave action and boring. This 2D model was the first step in
337 assessing the structural and mechanical consequences of high CO₂-induced changes to
338 growth structure, but it is important to note that it represented a 2D approximation of a
339 complex 3D structure. Here our results showed that a 3D extrapolation of the 2D FE-model
340 (Corridor model) generated comparable patterns and magnitudes of average stress to the 2D
341 model. However, once the complexity of the 3D model was altered to approximate cellular
342 compartments and compared to a biologically realistic model generated from SRXTM data, it
343 became clear that stress and strain energy magnitudes in the simple 2D and 3D models were
344 an over-estimation.

345 Coralline algae grow apically with lateral cell fusion being very common (Irvine and
346 Chamberlain, 1994). This creates a vast network of individual cells able to oppose stress in
347 all directions (Gordon, 1978). The importance of these structures is highlighted by the
348 geometric model with compartments (the Compartment model) being the most stable of the
349 geometric structures assessed and also most comparable – in terms of percentage volume of
350 calcite, stress distribution and magnitudes of average stress and total strain energy – to the
351 biological model (Table 1 & 2). This highlights the importance of geometry changes, which
352 our method accurately captured, to the distribution and magnitude of stress. This occurrence
353 was also observed by Romeed et al. (2006) who previously found that changes in the
354 geometry between their 2D and 3D models of a restored premolar tooth also affected their
355 displacement and profile stresses.

356 Creating the FE-model of the biologically realistic structure (the Biological model) from
357 SRXTM data was a time consuming process compared to the user effort required to generate
358 the compartmentalised geometric model (the Compartment model). As these different models
359 produced very similar measures of average stress ($2.75E+10$ Pa compared to $2.74E+10$ Pa for
360 the geometric and the biological model respectively), comparable measures of total strain
361 energy ($4.28E09$ J compared to $5.21E09$ J) and a similar stress distribution, we propose that
362 the compartment model presented a time efficient opportunity to manipulate geometric
363 features to test hypotheses of mechanical performance and structural integrity.

364 Hence this model was used to assess the impact of ocean acidification changes to the cell
365 growth on structural integrity. When the cellular size of the 3D model was adjusted to reflect
366 $589 \mu\text{atm}$ growth conditions, the structure was less 'efficient' than the structure under current
367 environmental conditions, with a higher average stress and total strain energy. It is important
368 to note that the increase in stress and total strain energy magnitude was less pronounced than
369 that suggested by the 2D models, indicating that the extra cellular walls aided in stabilising
370 the thinner cell walls of the model. This finding was in agreement with other work showing
371 that microstructural features affect the mechanical properties of cellular solids (Gibson,
372 2005). For example, wood has a stiffness to weight ratio equal to steel, which is partly due to
373 the arrangement of cells in a honeycomb structure (Gibson et al., 2010). Hence these features
374 provide habitat forming organisms with a larger structural integrity to withstand external
375 pressures and the ability to live in a highly dynamic environment such as the coastal shelf.

376 Although our geometric and biological models show congruence, they are still simplifications
377 of the heterogeneities in the algal skeleton. A factor which was not considered in this study is
378 the potential effect of changing material properties due to global change on the algal skeleton.
379 Material properties are affected by the concentration of Mg in the skeleton (Ma et al., 2008),
380 which is dependent on temperature (Kamenos et al., 2008) and potentially pH (Ragazzola et

381 al., 2013; Ries, 2011). Mg incorporated into the calcite lattice increases the lattice distortion,
382 which causes an increase in the sliding resistance and deformation resistance to crystals
383 (Wang et al., 1997). Ma et al. (2008) found that due to a much larger difference in mol% of
384 MgCO₃ (just below 40%), the high Mg-calcite polycrystalline matrix of the tooth of a sea
385 urchin had a significantly higher elastic modulus (E) and hardness (H) value than both
386 synthetic calcite and the single crystalline needles.

387 Sea surface temperatures in the North Atlantic are predicted to rise 2.5°C by the end of the
388 century (Rhein et al., 2013). This rise in temperature corresponds to a 3% increase in mol%
389 of MgCO₃ (Kamenos et al., 2008). As a 3% change in mol% of MgCO₃ is within the natural
390 variation between specimens (Ragazzola et al., 2013), we suggest such a mol% change in
391 MgCO₃ will not significantly impact the material properties and hence affect the skeleton .
392 However Ma et al. (2008) also suggested the large difference in material properties wasn't
393 due to just the difference in mol% of MgCO₃ but also due to the orientation and uniform size
394 of the crystals. This illustrates that Mg/Ca ratios are not the only factor which affects
395 material properties.

396 Proteins are also known to affect material properties as the incorporation of organic
397 macromolecules reduces the brittleness and enables plastic deformation (Berman et al., 1988;
398 Ma et al., 2008; Wang et al., 1997; Weiner et al., 2000). The presence of chitin and collagen
399 within the skeleton of *Clathromorphum compactum* aids calcification and increase skeletal
400 strength (Rahman and Halfar, 2014). Implementing accurate material properties specific for
401 specimens grown under a wide range of conditions into the model would allow a more
402 accurate assessment of whether phenotypic variability in material properties has the potential
403 to counteract structural changes in response to ocean acidification.

404 However, using these more biologically accurate models, we have further supported previous
405 results that state future climate change will lead to a loss in the structural integrity of coralline
406 algae. We have shown that by increasing the complexity of a simple 2D geometric model to a
407 3D geometric model we can obtain informative data on the effect of ocean acidification on
408 the structural integrity of the coralline algal skeleton, without need for complex real
409 biological models derived from CT scanning that take ample computer time to construct and
410 analyse. As responses to climate change are species-specific, we are therefore able to create
411 models tailor made to individual species and analyse how they react to future climate change.
412 We have also shown the susceptibility these models have to shear loads rather than
413 compressive loads.

414 As the oceans are becoming more acidic, with concurrent calcification pressure, it is vital to
415 understand the potential effect of ocean acidification on the skeletons of these habitat forming
416 organisms to infer whether they are able to maintain habitats in the future. As coralline algae
417 are major habitat formers, with the diversity and abundance of species dependent on their
418 structural complexity, weakening of the skeleton under high CO₂ conditions will affect the
419 organisms that rely on coralline algae as a habitat with important consequences for marine
420 ecosystems. Our model results, along with bioerosion, rising sea levels (Rhein et al., 2013)
421 and predicted increases in frequency and intensity of storm surges (Knutson et al., 2010)
422 strongly suggest that coralline algae will be under more intense environmental pressure in
423 future CO₂ scenarios.

424 It is important to note that recent long term studies have shown calcifying organisms
425 acclimating to ocean acidification for example cold water corals sustaining growth rates
426 (Form and Riebesell, 2012) or coralline algae decreasing growth rates to maintain cell wall
427 thickness (Ragazzola et al., 2013). The consequence of this sustained growth on the material

428 properties and structural integrity has not been assessed and poses an open question with
429 regards to their ability to provide habitats in the future.

430 AUTHOR CONTRIBUTIONS

431 Leanne Melbourne and Julia Griffin carried out the experiments under the guidance of
432 Daniela Schmidt and Emily Rayfield. Leanne Melbourne prepared the manuscript with
433 contributions from all co-authors.

434 ACKNOWLEDGEMENTS

435 The authors would like to thank NERC studentship award [NE/L501554/1] and the Natural
436 History Museum, London for LAM and a Royal Society URF for DNS for providing funding,
437 Federica Ragazzola for allowing access to FE-models and Jen Bright and Phil Anderson for
438 general help with modelling aspects. The tomographic scans from Ragazzola et al. (2012)
439 were taken on the TOMCAT beamline at the Swiss Light Source, Paul Scherrer Institut,
440 Villigen, Switzerland. European Commission under the 7th Framework Programme:
441 Research Infrastructures. We also would like to thank our reviewers, C. Evenhuis and an
442 anonymous reviewer, whose valuable comments provided improvements to our paper.

443 REFERENCES

- 444 Amado-Filho, G. M., Moura, R. L., Bastos, A. C., Salgado, L. T., Sumida, P. Y., Guth, A. Z., Francini-
 445 Filho, R. B., Pereira-Filho, G. H., Abrantes, D. P., Brasileiro, P. S., Bahia, R. G., Leal, R. N., Kaufman, L.,
 446 Kleypas, J. A., Farina, M., and Thompson, F. L.: Rhodolith Beds Are Major CaCO₃ Bio-Factories in the
 447 Tropical South West Atlantic, *PLoS ONE*, 7, e35171, 2012.
- 448 Andersen, L. and Jones, C.: Coupled boundary and finite element analysis of vibration from railway
 449 tunnels—a comparison of two-and three-dimensional models, *Journal of Sound and Vibration*, 293,
 450 611-625, 2006.
- 451 Andersson, A. J., Mackenzie, F. T., and Bates, N. R.: Life on the margin: implications of ocean
 452 acidification on Mg-calcite, high latitude and cold-water marine calcifiers, *Mar Ecol Prog Ser*, 373,
 453 265-273, 2008.
- 454 Berman, A., Addadi, L., and Weiner, S.: Interactions of sea-urchin skeleton macromolecules with
 455 growing calcite crystals - a study of intracrystalline proteins, *Nature*, 331, 546-548, 1988.
- 456 Brodie, J., Williamson, C. J., Smale, D. A., Kamenos, N. A., Mieszkowska, N., Santos, R., Cunliffe, M.,
 457 Steinke, M., Yesson, C., Anderson, K. M., Asnaghi, V., Brownlee, C., Burdett, H. L., Burrows, M. T.,
 458 Collins, S., Donohue, P. J. C., Harvey, B., Foggo, A., Noisette, F., Nunes, J., Ragazzola, F., Raven, J. A.,
 459 Schmidt, D. N., Suggett, D., Teichberg, M., and Hall-Spencer, J. M.: The future of the northeast
 460 Atlantic benthic flora in a high CO₂ world, *Ecology and Evolution*, 4, 2787-2798, 2014.
- 461 Caldeira, K. and Wickett, M. E.: Oceanography: anthropogenic carbon and ocean pH, *Nature*, 425,
 462 365-365, 2003.
- 463 Carrington, E.: Drag and dislodgment of an intertidal macroalga: consequences of morphological
 464 variation in *Mastocarpus papillatus* Kützinger, *Journal of Experimental Marine Biology and Ecology*,
 465 139, 185-200, 1990.
- 466 Ciais, P., Sabine, C., Bala, G., Bopp, L., Brovkin, V., Canadell, J., Chhabra, A., DeFries, R., Galloway, J.,
 467 Heimann, M., Jones, C., Quéré, C. L., Myneni, R. B., and Thornton, S. P. a. P.: Carbon and Other
 468 Biogeochemical Cycles. In: *Climate Change 2013: The Physical Science Basis. Contribution of Working*
 469 *Group I to the Fifth Assessment Report of the Intergovernmental Panel on Climate Change* (eds
 470 Stocker, T.F., Qin, D., Plattner, G.K., Tignor, M., Allen, S.K., Boschung, J., Nauels, A., Xia, Y., Bex, V.
 471 and Midgley, P.M.), Cambridge University Press, Cambridge, United Kingdom and New York, NY,
 472 USA., 2013.
- 473 Denny, M. W., Miller, L. P., Stokes, M. D., Hunt, L. J. H., and Helmuth, B. S. T.: Extreme Water
 474 Velocities: Topographical Amplification of Wave-Induced Flow in the Surf Zone of Rocky Shores,
 475 *Limnology and Oceanography*, 48, 1-8, 2003.
- 476 Diaz-Pulido, G., Gouezo, M., Tilbrook, B., Dove, S., and Anthony, K. R. N.: High CO₂ enhances the
 477 competitive strength of seaweeds over corals, *Ecology Letters*, 14, 156-162, 2011.
- 478 Dudgeon, S. R. and Johnson, A. S.: Thick vs. thin: thallus morphology and tissue mechanics influence
 479 differential drag and dislodgement of two co-dominant seaweeds, *Journal of Experimental Marine*
 480 *Biology and Ecology*, 165, 23-43, 1992.
- 481 Dumont, E., Grosse, I., and Slater, G.: Requirements for comparing the performance of finite element
 482 models of biological structures, *Journal of Theoretical Biology*, 256, 96-103, 2009.
- 483 Dumont, E. R., Piccirillo, J., and Grosse, I. R.: Finite-element analysis of biting behavior and bone
 484 stress in the facial skeletons of bats, *The Anatomical Record Part A: Discoveries in Molecular,*
 485 *Cellular, and Evolutionary Biology*, 283A, 319-330, 2005.
- 486 Fabricius, K. E., Langdon, C., Uthicke, S., Humphrey, C., Noonan, S., De'ath, G., Okazaki, R.,
 487 Muehllehner, N., Glas, M. S., and Lough, J. M.: Losers and winners in coral reefs acclimatized to
 488 elevated carbon dioxide concentrations, *Nature Climate Change*, 1, 165-169, 2011.
- 489 Form, A. U. and Riebesell, U.: Acclimation to ocean acidification during long-term CO₂ exposure in
 490 the cold-water coral *Lophelia pertusa*, *Global Change Biology*, 18, 843-853, 2012.
- 491 Foster, M. S.: Rhodoliths: between rocks and soft places, *Journal of Phycology*, 37, 659-667, 2001.

492 Foster, M. S., Amado Filho, G. M., Kamenos, N. A., Riosmena-Rodríguez, R., and Steller, D. L.:
493 Rhodoliths and Rhodolith Beds, *Smithsonian Contributions to the Marine Sciences*; no. 39, 2013.
494 143-155, 2013.

495 Freiwald, A. and Henrich, R.: Reefal coralline algal build-ups within the Arctic Circle: morphology and
496 sedimentary dynamics under extreme environmental seasonality, *Sedimentology*, 41, 963-984, 1994.

497 Gaylord, B., Blanchette, C. A., and Denny, M. W.: Mechanical Consequences of Size in Wave-Swept
498 Algae, *Ecological Monographs*, 64, 287-313, 1994.

499 Gibson, L. J.: Biomechanics of cellular solids, *Journal of Biomechanics*, 38, 377-399, 2005.

500 Gibson, L. J., Ashby, M. F., and Harley, B. A.: Cellular materials in nature and medicine, Cambridge
501 University Press, New York, 2010.

502 Gordon, J.: Structures: or Why Things Don't Fall Down, Penguin Books, New York, 1978.

503 Grall, J. and Hall-Spencer, J. M.: Problems facing maerl conservation in Brittany, *Aquatic
504 Conservation: Marine and Freshwater Ecosystems*, 13, S55-S64, 2003.

505 Irvine, L. M. and Chamberlain, Y. M.: Volume 1 Rhodophyta Part 2B Corallinales, Hildenbrandiales,
506 Natural History Museum, London, 1994.

507 Kamenos, N., Cusack, M., and Moore, P.: Coralline algae are global palaeothermometers with bi-
508 weekly resolution, *Geochimica et Cosmochimica Acta*, 72, 771-779, 2008.

509 Kamenos, N. A., Burdett, H. L., Aloisio, E., Findlay, H. S., Martin, S., Longbone, C., Dunn, J.,
510 Widdicombe, S., and Calosi, P.: Coralline algal structure is more sensitive to rate, rather than the
511 magnitude, of ocean acidification, *Global change biology*, 19, 3621-3628, 2013.

512 Knutson, T. R., McBride, J. L., Chan, J., Emanuel, K., Holland, G., Landsea, C., Held, I., Kossin, J. P.,
513 Srivastava, A., and Sugi, M.: Tropical cyclones and climate change, *Nature Geoscience*, 3, 157-163,
514 2010.

515 Kroeker, K. J., Kordas, R. L., Crim, R. N., and Singh, G. G.: Meta-analysis reveals negative yet variable
516 effects of ocean acidification on marine organisms, *Ecology letters*, 13, 1419-1434, 2010.

517 Ma, Y., Cohen, S. R., Addadi, L., and Weiner, S.: Sea Urchin Tooth Design: An "All-Calcite"
518 Polycrystalline Reinforced Fiber Composite for Grinding Rocks, *Advanced Materials*, 20, 1555-1559,
519 2008.

520 Mackenzie, F. T., Lerman, A., and Andersson, A. J.: Past and present of sediment and carbon
521 biogeochemical cycling models, *Biogeosciences*, 1, 11-32, 2004.

522 Nelson, W.: Calcified macroalgae—critical to coastal ecosystems and vulnerable to change: a review,
523 *Marine and Freshwater Research*, 60, 787-801, 2009.

524 Pörtner, H. O., Karl, D., Boyd, P. W., Cheung, W., Lluch-Cota, S. E., Nojiri, Y., Schmidt, D. N., and
525 Zavialov, P.: Ocean systems. In: *Climate Change 2014: Impacts, Adaptation, and Vulnerability. Part A:
526 Global and Sectoral Aspects. Contribution of Working Group II to the Fifth Assessment Report of the
527 Intergovernmental Panel of Climate Change* (eds Field, C.B., Barros, V.R., Dokken, D.J., Mach, K.J.,
528 Mastrandrea, M.D., Bilir, T.E., Chatterjee, M., Ebi, K.L., Estrada, Y.O., Genova, R.C., Girma, B., Kissel,
529 E.S., Levy, A.N., MacCracken, S., Mastrandrea, P.R. and

530 White, L.L.), Cambridge University Press, Cambridge, United Kingdom and New York, NY, USA, 411-
531 484 pp., 2014.

532 Ragazzola, F., Foster, L. C., Form, A., Anderson, P. S. L., Hansteen, T. H., and Fietzke, J.: Ocean
533 acidification weakens the structural integrity of coralline algae, *Global Change Biology*, 18, 2804-
534 2812, 2012.

535 Ragazzola, F., Foster, L. C., Form, A. U., Buscher, J., Hansteen, T. H., and Fietzke, J.: Phenotypic
536 plasticity of coralline algae in a High CO₂ world, *Ecology and Evolution*, 3, 3436-3446, 2013.

537 Rahman, M. A. and Halfar, J.: First evidence of chitin in calcified coralline algae: new insights into the
538 calcification process of *Clathromorphum compactum*, *Sci. Rep.*, 4, 2014.

539 Rayfield, E. J.: Finite element analysis and understanding the biomechanics and evolution of living
540 and fossil organisms, *Annu. Rev. Earth Planet. Sci.*, 35, 541-576, 2007.

541 Rhein, M., Rintoul, S., Aoki, S., Campos, E., Chambers, D., Feely, R., Gulev, S., Johnson, G., Josey, S.,
542 Kostianoy, A., Mauritzen, C., Roemmich, D., and Wang, L. T. a. F.: Observations: Ocean. In: *Climate*

543 Change 2013: The Physical Science Basis. Contribution of Working Group I to the Fifth Assessment
544 Report of the Intergovernmental Panel on Climate Change Cambridge University Press, Cambridge,
545 United Kingdom and New York, NY, USA, , 1535 pp., 2013.

546 Ries, J. B.: Skeletal mineralogy in a high-CO₂ world, *Journal of Experimental Marine Biology and*
547 *Ecology*, 403, 54-64, 2011.

548 Ries, J. B., Cohen, A. L., and McCorkle, D. C.: Marine calcifiers exhibit mixed responses to CO₂-
549 induced ocean acidification, *Geology*, 37, 1131-1134, 2009.

550 Romeed, S., Fok, S., and Wilson, N.: A comparison of 2D and 3D finite element analysis of a restored
551 tooth, *Journal of oral rehabilitation*, 33, 209-215, 2006.

552 Starko, S., Claman, B. Z., and Martone, P. T.: Biomechanical consequences of branching in flexible
553 wave-swept macroalgae, *New Phytologist*, 206, 133-140, 2015.

554 Tanur, A., Gunari, N., Sullan, R., Kavanagh, C., and Walker, G.: Insight into the composition,
555 morphology, and formation of the calcareous shell of the serpulid hydroides dianthus, *Journal of*
556 *Structural Biology*, 169, S5-S20, 2010.

557 Wang, R. Z., Addadi, L., and Weiner, S.: Design strategies of sea urchin teeth: structure, composition
558 and micromechanical relations to function, *Philosophical Transactions of the Royal Society of*
559 *London. Series B: Biological Sciences*, 352, 469-480, 1997.

560 Weiner, S., Addadi, L., and Wagner, H. D.: Materials design in biology, *Materials Science and*
561 *Engineering: C*, 11, 1-8, 2000.

562 Zienkiewicz, O., Taylor, Z., and Zhu, J.: *The finite element method: its basis and fundamentals.*
563 *Butterworth-Heinemann, Amsterdam, 2005.*

564

565 Tables

566 Table 1 Mesh type, number of elements, average von Mises Stress, 95th percentile of (Mises)

567 Stress and Total Strain energy for the different models

Model	Mesh type	Number of Elements	Average von Mises Stress (Pa)	95 percentile of von Mises Stress (Pa)	Total Strain Energy (J)
422 μatm 2D model	Quad	16368	1.67E+11		8.91E08
589 μatm 2D model	Quad	1889	5.17E+11		1.27E10
3D	hexagonal	202304	1.72E+11		1.11E11
3D*	hexagonal	202304			4.70E11
3D (Corridor model)	tetrahedral	2125549	7.46E+10	2.21E+11	1.75E10
422 μatm compartmentalised (Compartment model)	tetrahedral	3442433	2.75E+10	5.36E+10	4.28E09
589 μatm compartmentalised (OA model)	tetrahedral	1707673	4.98E+10		8.81E09
Biologically realistic model (Biological model)	tetrahedral	2106858	2.74E+10	5.63E+10	5.21E9

568 *Strain energy corrected for calcite volume

569 Table 2 Percentage volumes of calcite and cavities in the biological model, the corridor and

570 the compartment model.

	Biological Model	3D Corridor model	3D Compartment model
volume of calcite (μm^3)	3.09E+05	1.94E+05	2.87E+05
volume of cavities (μm^3)	1.83E+05	2.60E+05	1.67E+05
percentage of calcite	63%	43%	63%
percentage of cavities	37%	57%	37%

571

572

573 Table 3 Average von Mises Stress, 95th percentile of (Mises) Stress and Total Strain energy for the
 574 different load types exerted on the biological, compartment and corridor models. Total strain energy
 575 for the biological model has been corrected for calcite volume (equation 2). The compartment
 576 model under the shear loading type is highlighted to reiterate that the loading setup is different to
 577 the biological model under a shear loading type.

Model	Loading Type	Average Stress (N μm^{-2})	95th Percentile of (Mises) Stress (N μm^{-2})	Total Strain Energy (J)
Biological	Compressive	2.34E-04	4.08E-04	3.34E+05
	Shear	2.83E-04	6.07E-04	6.11E+05
	Original (Shear + Compressive)	3.49E-04	7.21E-04	9.73E+05
Compartment	Compressive	2.42E-04	2.96E-04	2.34E+05
	Shear	4.27E-04	1.03E-03	1.63E+06
	Original (Shear + compressive)	4.10E-04	8.25E-04	9.63E+05

578

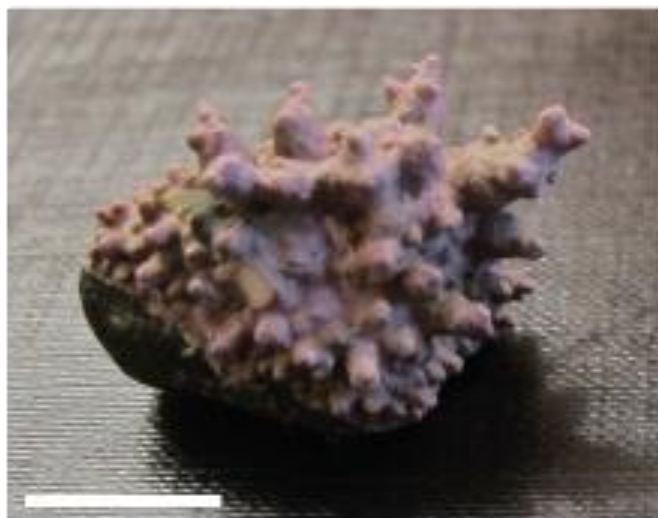
579 Table 4 Average von Mises Stress and Total Strain energy for the comparison of the different
 580 material properties in the 2D and 3D corridor models

	Young's Modulus (Pa)	Average Von Mises Stress (Pa)	Total Strain energy (J)
2D			
Calcite	3.60E+10	1.67E+11	8.91E+08
M.edulis -Min	4.39E+10	1.67E+11	7.30E+08
M.californianus -Min	4.79E+10	1.67E+11	6.69E+08
M.edulis -Max	7.18E+10	1.67E+11	4.47E+08
M.californianus -Max	7.93E+10	1.67E+11	4.04E+08
	Young's Modulus (Pa)	Average Von Mises Stress (Pa)	Total Strain energy (J)
3D corridor			
Calcite	3.60E+10	7.46E+10	1.75E+10
M.edulis -Min	4.39E+10	7.46E+10	1.43E+10
M.californianus -Min	4.79E+10	7.46E+10	1.31E+09
M.edulis -Max	7.18E+10	7.46E+10	8.77E+09
M.californianus -Max	7.93E+10	7.46E+10	7.94E+08

581

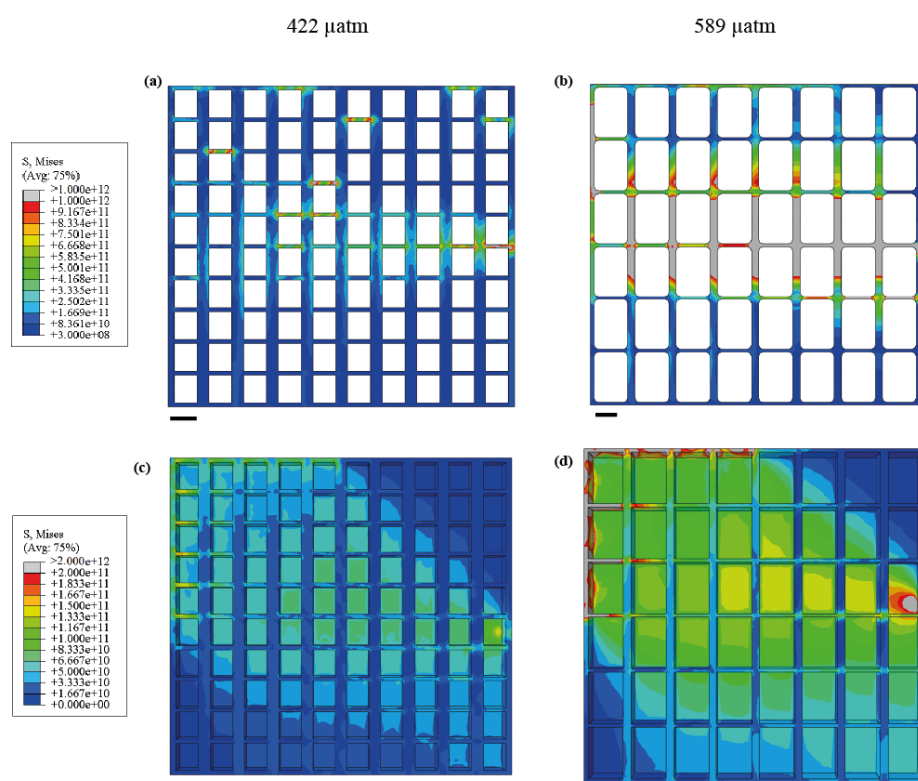
582 Figures

583 Figure 1



584

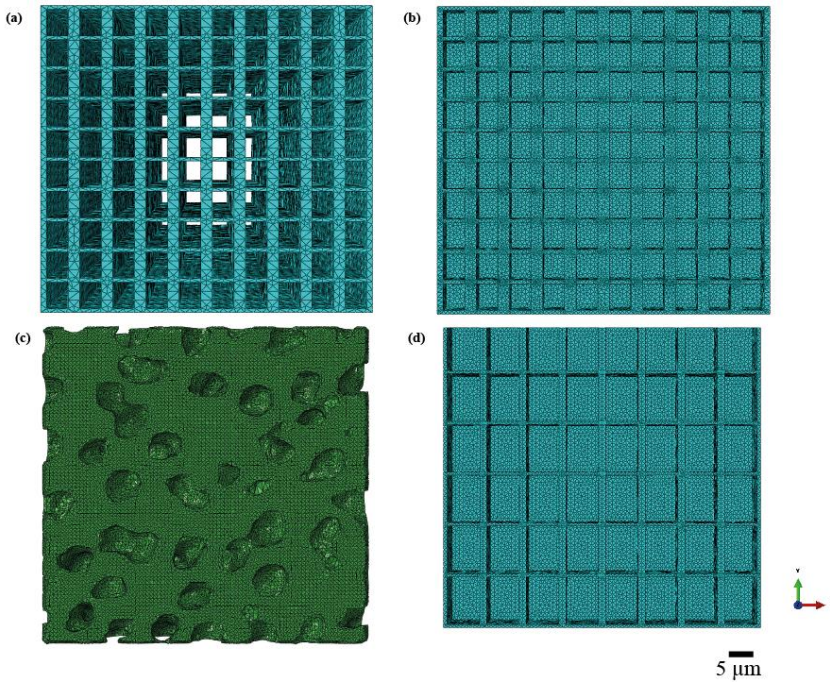
585 Figure 2



586

587

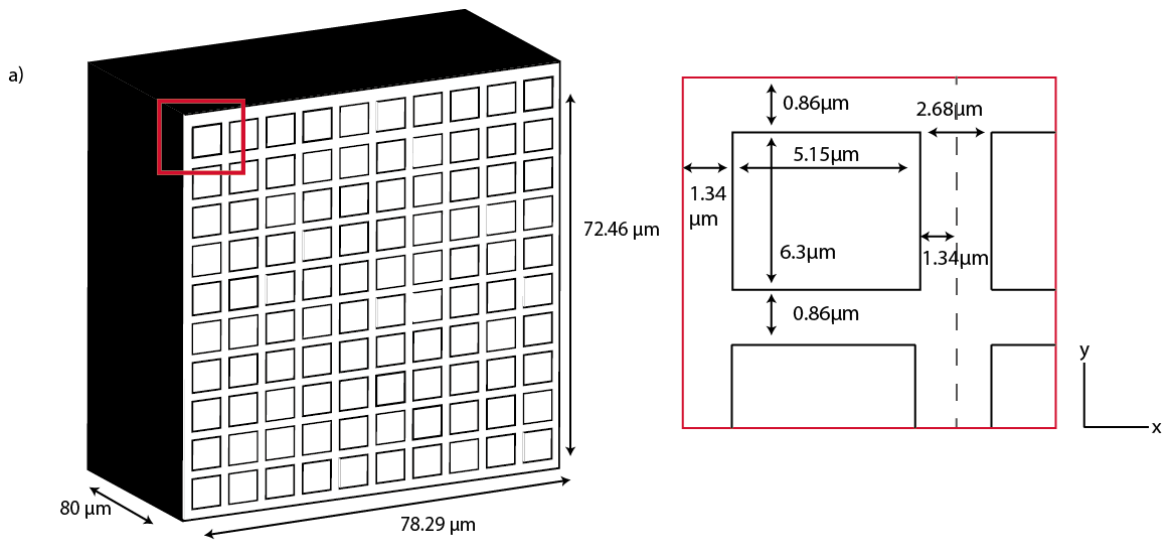
588 Figure 3



589

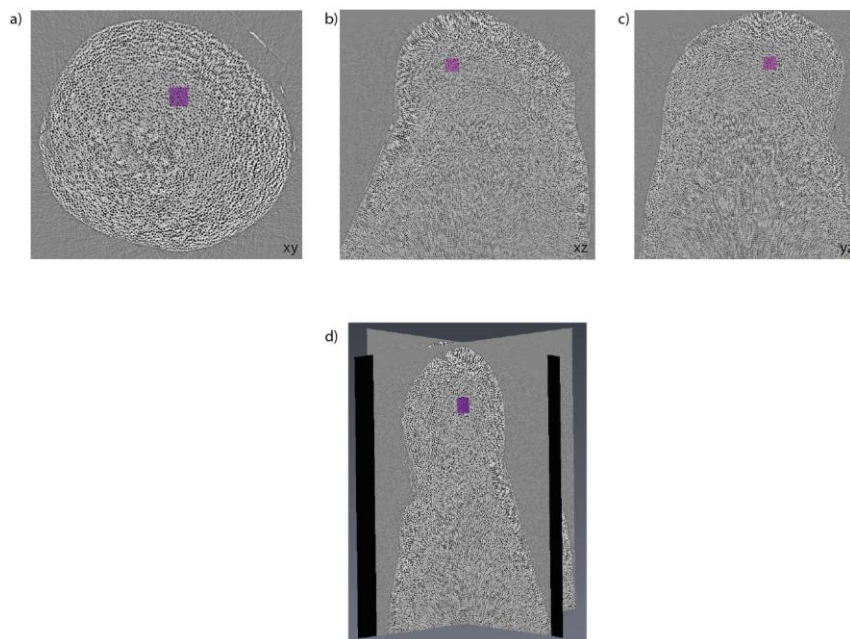
590 Figure 4

591



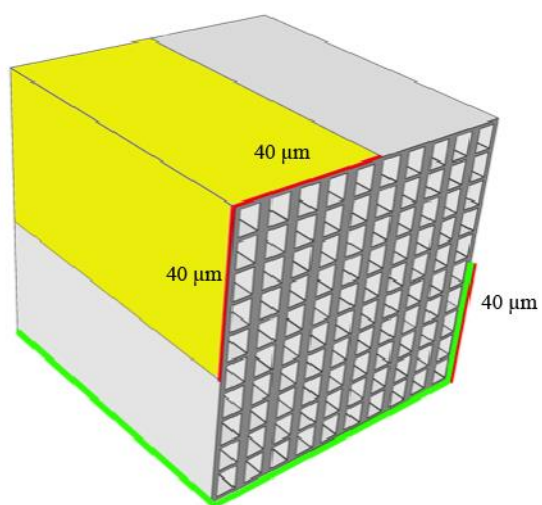
592

593 Figure 5



594

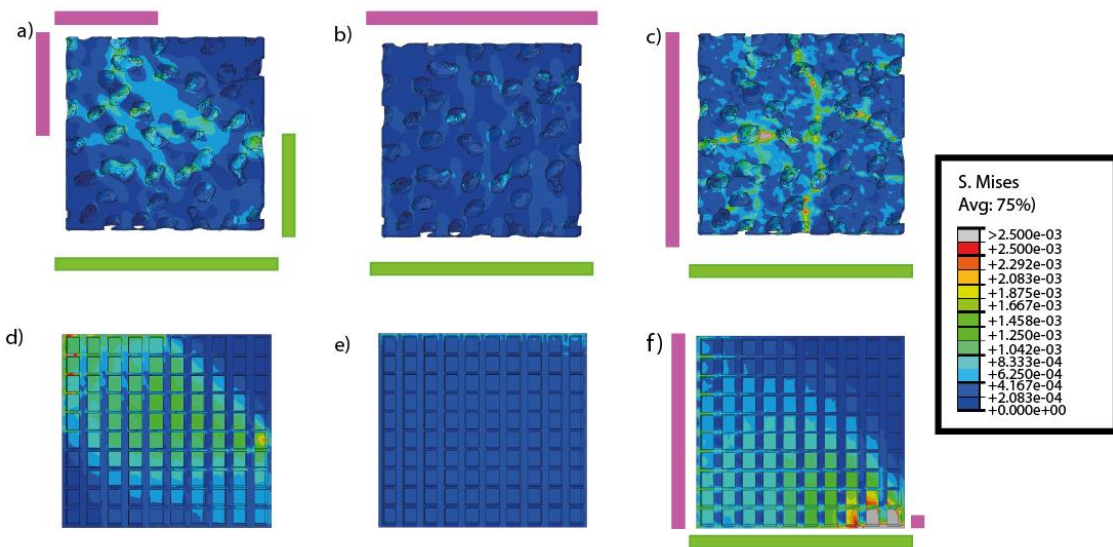
595 Figure 6



596

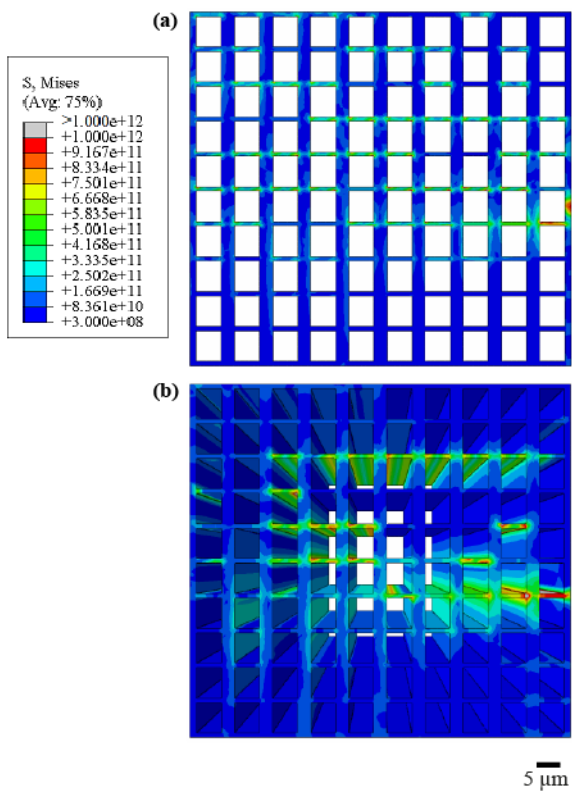
597

598 Figure 7



599

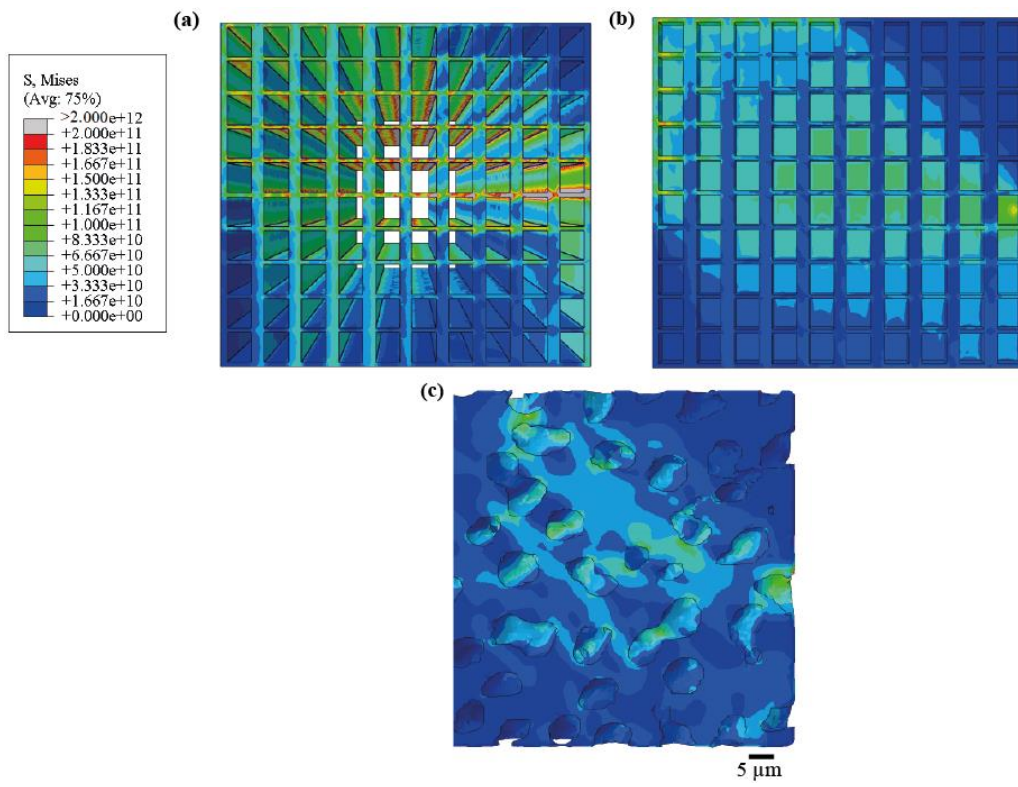
600 Figure 8



601

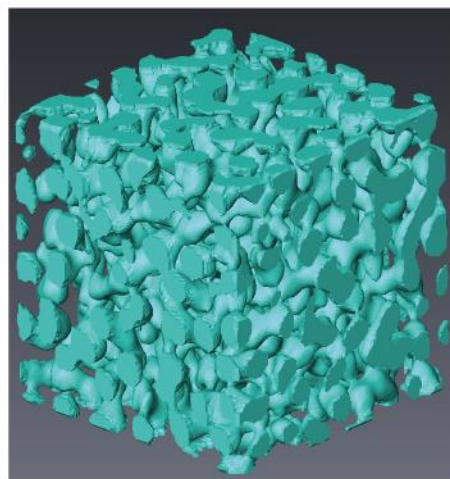
602

603 Figure 9



604

605 Figure 10



606

607

608 Figure Legends

609 Figure 1: A *Lithothamnion glaciale* specimen in crustose form from Loch Creran, Oban,
610 Scotland; Scale = 1cm.

611 Figure 2: The effect of elevated CO₂ on the *Lithothamnion glaciale* structure. All models are
612 subjected to the same loads and boundary conditions and measurements taken from
613 Ragazzola et al. (2012). Von Mises Stresses are projected onto the 2D Finite element model
614 (a, b) and the 3D compartmentalised models (c, d). Warm colours indicate areas of high
615 stress, while cooler blue colours indicate areas of low stress. Units = Pa
616 Figure 3: The four
617 computer derived models; (a) The Corridor model, a simple 3D model; (b) The Compartment
618 model, a compartmentalised model; (c) The Biological model, the biologically realistic
619 model; (d) The OA model, the compartmentalised model under pCO₂ conditions simulating
the year 2050

620 Figure 4: Dimensions used in the 3D corridor model. Units = μm

621 Figure 5: Orthoslice projections in the different planes of a rhodolith thallus: a) xy direction;
622 b) xz direction; c) yz direction and d) in 3D format. The purple box highlights where the
623 80 μm x 80 μm cube was selected.

624 Figure 6: Loads and Boundary constraints. All models had the same loads and constraints
625 applied. Loads, representing wave erosion, were applied to the top left hand corner along a
626 strip 40 μm wide at the external top left side of the model (yellow surface). Constraints were
627 applied to the bottom right corner (opposite corner to load) along a strip 40 μm wide up the
628 right hand side of the model and over the whole of the bottom model (green lines).

629 Figure 7: The von Mises Stress patterns on the biological model (a, b & c) and the
630 compartment model (d, e & f) in different loading situations; the original (mixture of both

631 shear and compressive loads) (a & d); compressive load (b & e) and the shear load (c & f).

632 The different load situations (pink box) are shown on the biological model as well as the

633 constraints (green boxes). The shear load for the compartment model was set up slightly

634 differently and hence the loading setup is displayed on the model (f). Units = $\text{N } \mu\text{m}^{-2}$.

635 Figure 8: (a) 2D vs (b) 3D comparison of the *Lithothamnion glaciale* structure based on

636 Ragazzola et al. (2012) measurements. Units = Pa

637 Figure 9: Comparison of all 3D models. (a) The 3D corridor model (b) the compartment

638 model and (c) the biological model. Units = Pa.

639 Figure 10: The inside spheroidal cavities of the biological model